Chemical Science

ROYAL SOCIETY OF CHEMISTRY

EDGE ARTICLE

View Article Online
View Journal

Cite this: DOI: 10.1039/d6sc02594c

All publication charges for this article have been paid for by the Royal Society of Chemistry

A highly stable, planar thiophene-fused triarylborane as a new building block for semiconductor polymers

Yohei Adachi, *[a] Ryuji Matsuura,[a] Hiroki Tobita,[a] Tsubasa Mikie, [b] Itaru Osaka [b] and Joji Ohshita *[ac]

π-Conjugated compounds containing tricoordinate boron atoms have attracted significant attention because of their unique properties, including low-lying LUMO energy levels, extended π-conjugation, and high Lewis acidity. In particular, planarized triarylboranes have been extensively studied in recent years owing to their high chemical stability and excellent photoluminescence properties. Despite exhibiting potential for strong intermolecular interactions and superior semiconducting performance arising from the absence of bulky substituents, the synthesis of p–π* conjugated polymers using such planarized units as building blocks, along with the evaluation of their semiconducting properties, remains a significant challenge that has not yet been addressed. In this study, we report the synthesis of **DTTB**, a new planarized triarylborane featuring benzene and thiophene rings fused *via* boron and sulfur atoms. **DTTB** represents a versatile building block that combines good chemical stability with a perfectly planar geometry, facilitating intermolecular π–π stacking as confirmed by X-ray crystallography. Furthermore, the fused thiophene rings allowed for facile deprotonation at the α-positions, enabling the first integration of planarized triarylborane units into p–π* conjugated polymers. The synthesized p–π* conjugated polymers exhibited ambipolar transport behavior with enhanced carrier mobilities compared to non-planarized analogs. This work provides a conceptual advance by demonstrating that the rigid planarization of triarylborane units is a superior strategy for enhancing the semiconducting performance and thermal stability of p–π* conjugated materials, offering a design strategy for polymer semiconductors.

Received 30th March 2026
Accepted 26th May 2026

DOI: 10.1039/d6sc02594c

rsc.li/chemical-science

Introduction

The introduction of main group elements into π-conjugated systems has been utilized to develop various functional materials, as it induces unique changes in photophysical properties. For instance, the incorporation of nitrogen or sulfur is known to elevate the highest occupied molecular orbital (HOMO) energy level of compounds. Therefore, these elements are widely employed in p-type semiconductor materials.[1] Among main group elements, the introduction of tricoordinate boron causes particularly unique optoelectronic properties. Incorporating a tricoordinate boron atom into a π-conjugated system effectively and selectively lowers the lowest unoccupied molecular orbital (LUMO) energy level of the compound. This phenomenon arises from the p–π* interaction between the vacant p-orbital of the boron atom and the π*-orbital of the adjacent π-system (Fig. 1a). Furthermore, the inherent Lewis acidity of tricoordinate boron allows for interaction with Lewis bases, such as anions, which disrupts this p–π* conjugation, resulting in significant alterations in their optical properties. Moreover, by combining tricoordinate boron with Group 15 and 16 elements such as nitrogen or sulfur, it is possible to control intramolecular donor–acceptor interactions and aromaticity. Because of these intriguing characteristics, tricoordinate boron-containing π-conjugated systems have been extensively explored for applications in functional materials,[2] including n-type semiconductors.[3] However, a significant challenge remains: tricoordinate boron compounds typically exhibit hydrolytic instability, necessitating robust stabilization strategies for practical application. The most prevalent strategy is kinetic stabilization *via* the introduction of bulky substituents, such as mesityl or tripyl groups, onto the boron atom (Fig. 1a). While this method reliably enhances stability, the steric hindrance imposed by these bulky groups often suppresses intermolecular interactions in the solid state, thereby limiting semiconductor performance. Consequently, reports of p–π* conjugated materials that exhibit excellent semiconductor

[a]*Smart Innovation Program, Graduate School of Advanced Science and Engineering, Hiroshima University, Higashi-Hiroshima 739-8527, Japan. E-mail: yadachi@hiroshima-u.ac.jp; jo@hiroshima-u.ac.jp*

[b]*Applied Chemistry Program, Graduate School of Advanced Science and Engineering, Hiroshima University, Higashi-Hiroshima 739-8527, Japan*

[c]*Division of Materials Model-Based Research, Digital Monozukuri (Manufacturing) Education and Research Center, Hiroshima University, Higashi-Hiroshima, Hiroshima 739-0046, Japan*

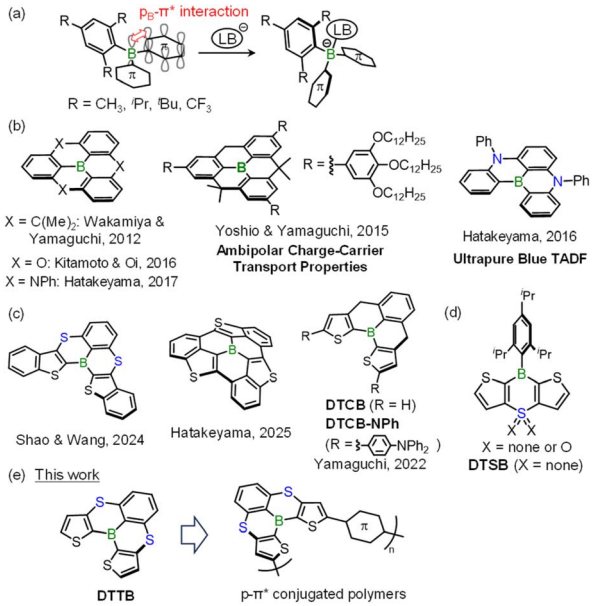

Fig. 1 (a) Electronic characteristics of tricoordinate boron *via* p–π* interaction. (b and c) Structures of previously reported planarized triarylboranes. (d) Chemical structure of **DTSB**. (e) Structure of the planarized triarylborane **DTTB** synthesized in this study.

properties remain scarce, leaving significant room for improvement.[3]

In 2012, Yamaguchi and co-workers pioneered a stabilization strategy for triarylboranes by bridging the three aryl groups surrounding the boron atom, effectively locking the molecule into a planar conformation (Fig. 1b).[4] This structural rigidity inhibits structural deformation toward a tetracoordinate state, imparting kinetic stability. In addition to exceptional chemical stability, these planarized triarylboranes can be tailored with unique properties depending on the bridging heteroatoms.[5] For instance, Hatakeyama and co-workers demonstrated that using nitrogen as a bridging element induces a multiple resonance (MR) effect, yielding molecules with outstanding thermally activated delayed fluorescence (TADF) (Fig. 1b).[5b] Following this discovery, numerous planarized triarylboranes with superior luminescence properties were reported.[6] However, current research on planarized triarylboranes remains heavily focused on their luminescence (TADF) properties,[7] and the structural advantages of these rigid, inherently planar frameworks for electronic applications have been largely overlooked. Although the high planarity and absence of bulky substituents are expected to facilitate strong intermolecular π–π interactions, to the best of our knowledge, there are no precedents for investigating the semiconducting properties of conjugated polymers incorporating such skeletons, except for small-molecule systems.[8]

Thiophene is one of the most frequently used building blocks for π-conjugated systems owing to its superior chemical and thermal stability and the ease of selective functionalization. Accordingly, compounds combining thiophene rings with tricoordinate boron have been widely investigated.[9] Nevertheless, examples of planarized boron compounds fused to thiophene rings remain limited (Fig. 1c).[10] Although benzothiophene is used in some cases, π-extension *via* the thiophene ring is not possible in these situations.[10a,c] An exception is planarized borane (**DTCB**, Fig. 1c) featuring methylene-bridged thiophene and benzene rings; this unit allows for the extension of π-conjugation from the thiophene rings.[10b] We previously synthesized p–π* conjugated polymers using a building block containing a thiaborin ring fused to thiophene rings (**DTSB**, Fig. 1d).[11] However, owing to the bulky substituents on the boron atom, thin films of these polymers failed to exhibit carrier transport properties.[11c] In this study, we report a conceptual advance in the design of tricoordinate boron materials by synthesizing **DTTB**, in which two thiophene rings and a benzene ring are bridged by sulfur atoms across the boron center, and demonstrating its potential as a building block for semiconductor polymers. Unlike traditional triarylboranes that rely on bulky groups for kinetic stabilization, the **DTTB** unit achieves high chemical stability through rigid planarization, which simultaneously enables intermolecular π–π stacking. By leveraging the thiophene rings as synthetic handles, we achieved the first synthesis of p–π* conjugated polymers incorporating such planarized triarylborane cores. These polymers exhibited significantly enhanced carrier mobilities compared to their non-planarized counterparts, suggesting that planarization is an effective strategy for unlocking the semiconducting potential of boron-containing π-conjugated polymers.

Results and discussion

Synthesis and characterization

The synthetic pathway to **DTTB** is depicted in Fig. 2a. Initially, the 2-position of 1,3-dibromobenzene was deprotonated using lithium diisopropylamide (LDA), and a trimethylsilyl group was introduced. This silyl group introduction was critical for enhancing the reactivity of the *ipso*-carbon at the 2-position for the subsequent bromination. The two bromo groups were subsequently converted *via* stepwise thioetherification involving lithiation followed by nucleophilic substitution with bis(3-thienyl)disulfide. Precursor **4** was then prepared through the tribromination of **3** with *N*-bromosuccinimide (NBS). Subsequent trilithiation of **4**, followed by treatment with trimethyl borate, afforded the target compound, **DTTB**, in 60% yield. Consistent with our expectations, **DTTB** exhibited high chemical stability and remained stable under ambient conditions for extended periods, with no noticeable degradation. The ^{11}B NMR spectrum of **DTTB** displayed a broad signal at 37 ppm, confirming the tricoordinate nature of the boron center. To confirm the molecular structure, single-crystal X-ray diffraction analysis was performed on crystals obtained *via* the slow evaporation of a CH_2Cl_2/ethanol solution. As shown in Fig. 2b, the sum of the C–B–C bond angles in **DTTB** is 360.0°, validating its perfectly planar conformation. Moreover, the crystal packing exhibits a distinct π-stacking arrangement with an intermolecular distance of 3.52 Å (Fig. 2c), demonstrating that the elimination of bulky substituents on the boron atom effectively promotes intermolecular π–π interactions.

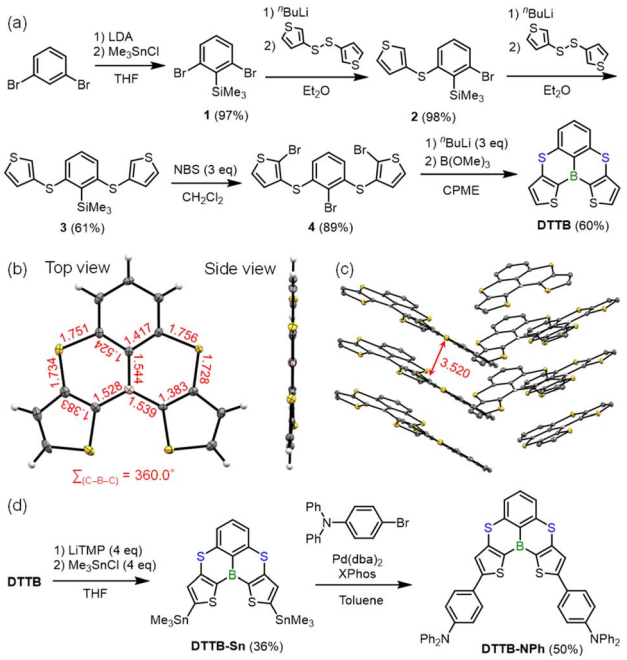

Fig. 2 (a) Synthetic route for DTTB. (b) Single-crystal X-ray structure of DTTB measured at 100 K and (c) its corresponding packing structure. Bond lengths and intermolecular distances are given in Å. Thermal ellipsoids are set at the 50% probability level. Hydrogen atoms in the packing structure are omitted for clarity. (d) Reaction pathway for the π-extension of DTTB *via* sequential lithiation and Stille coupling reactions.

Efforts were then directed toward modifying the outer α-positions of the thiophene rings in **DTTB** to introduce functional groups for further π-extension. Although an Ir-catalyzed direct C–H borylation was previously reported for **DTCB**,[10b] this reaction failed to proceed with **DTTB** under identical conditions. Consequently, a lithiation approach was explored (Fig. 2d). Treatment with *n*-butyllithium or lithium diisopropylamide (LDA) resulted in complex mixtures. In contrast, the use of a bulky base, lithium tetramethylpiperidide (LiTMP), promoted the desired lithiation. Subsequent quenching with trimethyltin chloride afforded the distannylated derivative, **DTTB-Sn**, in 36% yield. As a model reaction, the Stille coupling reaction of **DTTB-Sn** with 4-bromotriphenylamine afforded the diphenylaminophenyl-substituted compound, **DTTB-NPh**, in 50% yield. These results demonstrate that both functionalization and extension of the π-conjugation of **DTTB** are achievable *via* sequential lithiation and Stille coupling reactions.

Optical and electrochemical properties

The optical properties of **DTTB** and **DTTB-NPh** were characterized (Fig. 3). In toluene, **DTTB** and **DTTB-NPh** exhibit absorption maxima at 423 nm and 470 nm, respectively. The absorption maximum of **DTTB** shows a significant bathochromic shift relative to that of **DTCB** (λ_{abs} = 330 nm in toluene).[10b] This shift is likely caused by the destabilization of the HOMO energy level owing to the electron-donating nature of the bridging sulfur atoms. A red shift was also observed relative to

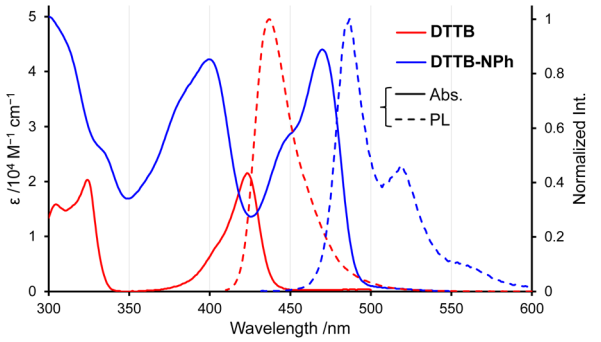

Fig. 3 UV-vis absorption and PL spectra of DTTB and DTTB-NPh in toluene at 0.01 mM.

DTSB (λ_{abs} = 347 nm in THF),[11b] which can be attributed to the extended π-conjugation resulting from the improved coplanarity of the benzene and thiophene rings in **DTTB**. The further red shift in **DTTB-NPh** suggests effective extension of the π-conjugation and significant donor–acceptor interactions.

In toluene, **DTTB** exhibits blue photoluminescence (PL) with a peak maximum at 437 nm (Fig. 3). The Stokes shift of **DTTB** is 757 cm^{-1}, smaller than that of **DTCB** (1894 cm^{-1}).[10b] Furthermore, the full width at half maximum (FWHM) is very narrow at 28 nm. These results indicate that **DTTB** possesses a highly rigid structure that undergoes minimal structural relaxation in the S_1 state. The PL lifetime is 2.48 ns, confirming its fluorescent nature. The PL spectra and lifetimes of **DTTB** were virtually unaffected by solvent polarity (Fig. 4a, S1a, and Table 1), indicating that the intramolecular charge transfer (ICT) character in the excited state is negligible. Despite its high structural rigidity, the PL quantum yield (Φ_{PL}) of **DTTB** is moderate at 19% in toluene (Table 1). Given that boron/nitrogen hybrid systems often exhibit efficient TADF due to the MR effect,[7] we investigated the potential TADF properties of structurally similar **DTTB**. Because TADF originates from the S_1 state populated *via* reverse intersystem crossing (RISC) from the T_1 state, it is typically susceptible to quenching by atmospheric oxygen.[12] Comparison of the PL spectra of a toluene solution of **DTTB** before and after deaeration revealed negligible changes (Fig. S2), confirming that **DTTB** does not exhibit TADF. To determine the underlying cause, the PL spectra of a **DTTB**-doped (1 wt%) PMMA film were measured at room temperature and 77 K (Fig. S3). At room temperature, a fluorescence band was observed at 442 nm, similar to the PL in toluene. In

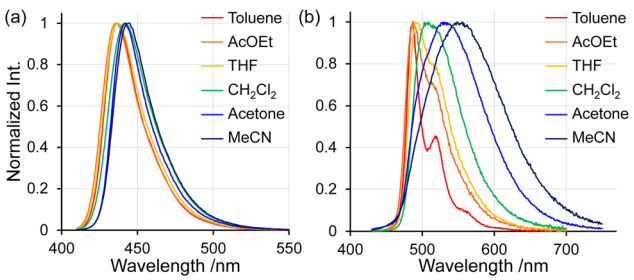

Fig. 4 PL spectra of DTTB (a) and DTTB-NPh (b) in various solvents at 0.01 mM.

Table 1 Optical properties of DTTB and DTTB-NPh in various solvents

Compound	Solvent	λ_{abs}/nm [a]	λ_{PL}/nm [b]	Φ_{PL}/% [c]	τ/ns [d]
DTTB	Toluene	423	437	19	2.48
	AcOEt	—	436	21	2.54
	THF	—	437	10	2.69
	CH_2Cl_2	—	442	10	3.34
	Acetone	—	442	20	3.43
	MeCN	—	444	19	3.89
DTTB-NPh	Toluene	470	487	14	0.71
	AcOEt	—	487	18	0.83
	THF	—	490	17	0.70 (18%), 0.90 (82%)
	CH_2Cl_2	—	509	19	0.89 (75%), 1.22 (25%)
	Acetone	—	530	23	1.48 (78%), 3.50 (22%)
	MeCN	—	556	3	1.99 (57%), 3.04 (43%)

[a] Absorption maxima. [b] PL maxima. [c] Absolute PL quantum yield. [d] PL lifetimes. Values in parentheses represent the percentage lifetime contribution of each component.

contrast, at 77 K, a new PL band appeared at 505 nm in addition to the fluorescence band. The lifetime of this new band was determined to be 157 ms (Fig. S4), confirming its assignment as phosphorescence. The energy difference between the S_1 and T_1 states (ΔE_{ST}), calculated from the onsets of these two PL bands, is relatively large at 0.40 eV, which explains the absence of TADF in **DTTB**. Similar relatively large ΔE_{ST} values were reported for benzothiophene analogs.[10c] The large ΔE_{ST} value of **DTTB** compared with those of analogous planarized boron compounds[5b,7] may stem from the lower aromaticity of thiophene than benzene, which promotes greater electron delocalization across the entire molecule. Such delocalization likely reduces the spatial separation of HOMO and LUMO on specific atoms, thereby weakening the MR effect. Further details on this point are provided in the DFT calculations section. The observation of intense phosphorescence at 77 K suggests that intersystem crossing (ISC) from the S_1 to the T_1 state occurs efficiently even at room temperature, thereby competing with fluorescence and reducing Φ_{PL}.

The observed PL maximum of **DTTB-NPh** in toluene at 487 nm showed a significant bathochromic shift relative to that of **DTTB**, consistent with the absorption spectra. In contrast to **DTTB**, the PL spectra of **DTTB-NPh** exhibited a red shift with increasing solvent polarity (Fig. 4b and Table 1), indicating the formation of an ICT excited state in polar solvents. This implies that the diphenylaminophenyl groups act as donors and the **DTTB** unit as an acceptor, suggesting that the **DTTB** unit possesses intrinsic electron deficiency stemming from the tricoordinate boron atom. On the other hand, the difference between the ground- and excited-state dipole moments ($\Delta\mu$) for **DTTB-NPh**, determined from a Lippert–Mataga plot[13] (Fig. S5), is 11.1 D. This value is approximately half that of **DTCB-NPh** (20.9 D, Fig. 1c),[10b] suggesting that the electron-accepting ability of the **DTTB** unit is attenuated by the electron-donating character of the sulfur atoms.

To determine the frontier orbital energies, cyclic voltammetry (CV) was performed. Neither **DTTB** nor **DTTB-NPh** exhibited reduction waves within the potential window, indicating the relatively low electron deficiency of the **DTTB** unit, consistent with the aforementioned discussion. On the other hand, clear oxidation waves were observed for both compounds (Fig. S6). The HOMO energy levels of **DTTB** and **DTTB-NPh** were estimated from their onset potentials to be −5.48 and −5.12 eV, respectively. The relatively high-lying HOMO energy level of **DTTB** can be ascribed to the electron-donating sulfur atoms, whereas the further increase in the HOMO energy level of **DTTB-NPh** is due to the electron-donating triphenylamine groups.

DFT calculations

Density functional theory (DFT) calculations were performed to gain insight into the electronic states of these compounds. Consistent with the single-crystal X-ray diffraction results, the optimized geometry of **DTTB** was found to be perfectly planar, with the sum of the C–B–C bond angles totaling 360.0° (Fig. 5a). The HOMO of **DTTB** is primarily located on the aromatic rings and the sulfur atom, whereas the LUMO is principally

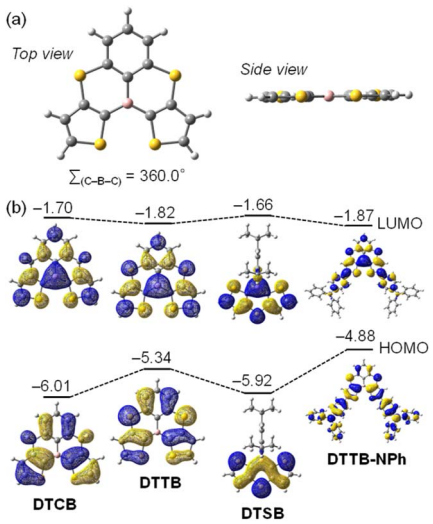

Fig. 5 (a) Optimized geometry of DTTB and (b) frontier molecular orbitals of planarized triarylboranes calculated at the B3LYP/6-31G(d) level.

concentrated on the boron atom (Fig. 5b). The LUMO energy level of **DTTB** was calculated to be lower than that of **DTSB**, indicating that planarization effectively lowers the LUMO energy level while extending the π-conjugation. Furthermore, the presence of electron-donating sulfur atoms significantly destabilizes the HOMO of **DTTB** compared with that of the methylene-bridged analog **DTCB**, corroborating the experimental absorption and CV data. For **DTTB-NPh**, the HOMO is delocalized over the entire molecule, including the triphenylamine unit. In contrast, the LUMO remains localized on the **DTTB** core, confirming that the **DTTB** unit functions as a weak acceptor. TD-DFT calculations revealed that for both **DTTB** and **DTTB-NPh**, the $S_0 \rightarrow S_1$ transition is primarily attributed to the HOMO → LUMO transition (Fig. S7 and Table S1). For **DTTB-NPh**, the long-wavelength absorption band was found to correspond to a transition with CT character. The higher-energy absorption bands were assigned to the HOMO−1 → LUMO and HOMO → LUMO+1 transitions for both compounds. Next, nucleus-independent chemical shift (NICS) calculations[14] were performed to evaluate aromaticity (Table S2). The NICS(1) value for the thiaborin ring of **DTSB** is −4.44, suggesting moderate aromaticity, whereas that of **DTTB** is −2.14, indicating reduced aromaticity. This reduction likely results from the fusion of the highly aromatic benzene ring to the thiaborin core. Nonetheless, the NICS(1) value of **DTTB** remains more negative than that of the non-aromatic dihydroborin ring in **DTCB** (−0.34), indicating the presence of residual aromaticity, which likely contributes to the enhanced stability of **DTTB**. This trend is also consistent with the $NICS(1)_{zz}$ results.

To further elucidate the influence of the fused aromatic rings, the ΔE_{ST} values were compared (Fig. S8). In agreement with experimental observations,[5b,15] the theoretical ΔE_{ST} (ΔE_{ST}^{DFT}) value of **DTTB** is larger than those of analogous planarized boranes featuring fused benzene rings, consistent with the absence of TADF in **DTTB**. Detailed molecular orbital analysis revealed that the HOMO of **DTTB** is delocalized on the C=C double bonds of the thiophene rings. This substantial HOMO–LUMO overlap in this region is likely responsible for the increased ΔE_{ST} in **DTTB**. Furthermore, computational analysis of several additional systems revealed that while the bridging elements (nitrogen or sulfur) linking the aromatic rings exert minimal influence on ΔE_{ST}^{DFT}, the ΔE_{ST}^{DFT} values tend to increase significantly as the aromaticity of the fused rings decreases in the order of benzene > thiophene > furan (Fig. S8). Additionally, the orientation of ring fusion had a negligible effect in the case of **DTTB**. These results suggest that the selection of fused rings is the most critical factor for controlling the TADF and phosphorescence properties of planarized boranes.

Investigation of Lewis acidity

Triarylboranes typically exhibit Lewis acidity, leading to their investigation for use in catalysts and sensor materials. To explore how the structural features of **DTTB** influence the Lewis acidity of the boron center, titration experiments were conducted using pyridine as a Lewis base. Upon the addition of

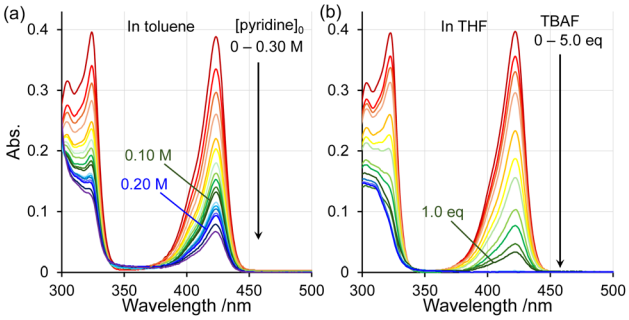

Fig. 6 UV-vis absorption spectral changes of DTTB (0.02 mM) upon the addition of (a) pyridine and (b) TBAF.

pyridine to a toluene solution of **DTTB**, the absorption band at 423 nm gradually decreased (Fig. 6a), indicating the coordination of pyridine to the boron center. The association constant (K_a) was determined to be 19 M^{-1} from the resulting titration curve (Fig. S9).[16] This relatively small value indicates that the Lewis acidity of **DTTB** is reduced upon planarization, consistent with observations for other planarized triarylborane derivatives.[6c,10a] Furthermore, given that K_a for **DTCB** is reported as 90 M^{-1},[10b] the lower K_a value for **DTTB** suggests that electron donation from the sulfur atoms to the empty p-orbital of boron further attenuates its Lewis acidity. Although **DTTB** is a relatively weak Lewis acid, titration experiments with tetra-*n*-butylammonium fluoride (TBAF) revealed that it forms an adduct nearly quantitatively with anions that form strong bonds with boron, such as the fluoride ion (Fig. 6b). This coordination proceeded rapidly, and the spectral changes were nearly complete immediately upon the addition of the bases (Fig. S10). For a more detailed evaluation, fluoride ion affinity (FIA) calculations[17] were performed. Despite the lack of bulky substituents, **DTTB** exhibits an FIA value (281 kJ mol^{-1}) that is nearly identical to that of **DTSB** (283 kJ mol^{-1}), indicating comparable Lewis acidity between the two (Table S3). The calculated FIA values for **DTTB** and **DTCB** are also comparable, a result that does not strictly align with the experimental trend observed in the K_a values of pyridine. This discrepancy is likely attributable to the differences in the steric requirements of the Lewis bases or to solvent effects. In any case, the calculated FIA value of **DTTB** is considerably smaller than that of tris(pentafluorophenyl)borane (449 kJ mol^{-1}), further supporting the relatively modest Lewis acidity of the **DTTB** framework.

Synthesis and properties of organic semiconductor polymers

Tricoordinate boron-containing π-conjugated systems are promising candidates for n-type semiconductors owing to their inherent electron-deficient nature. We synthesized electron-deficient p–π* conjugated polymers by subjecting **DTTB-Sn** to Stille coupling copolymerization with common acceptor units, such as naphthalenediimide (NDI) and diketopyrrolopyrrole (DPP) (Scheme 1). The properties of the resulting polymers, **P1** (the NDI copolymer) and **P2** (the DPP copolymer), were characterized after purification *via* reprecipitation, as summarized in Table 2. **P2** achieved a high number-average molecular

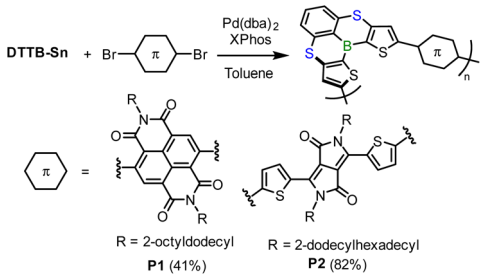

Scheme 1 Synthetic route for electron-deficient p–π* conjugated polymers utilizing a DTTB unit as a building block.

weight (M_n) of 32,600, whereas **P1** had a relatively low M_n of 7,500. This difference is attributed to the fact that **P2** exhibited a monomodal molecular weight distribution, whereas **P1** showed a bimodal distribution containing a low-molecular-weight fraction (Fig. S11), which could not be separated by reprecipitation. Thermogravimetric analysis (TGA) revealed 5% weight-loss temperatures (T_d^5) of 450 °C for **P1** and 424 °C for **P2**. Notably, these values are more than 70 °C higher than that of a previously reported copolymer of DTSB and DPP (354 °C),[11c] demonstrating that planarization of the triarylborane unit significantly enhances the thermal stability of these p–π* conjugated systems.

The absorption maxima for **P1** and **P2** in chloroform solutions were observed at 605 nm and 644 nm, respectively (Fig. 7a). These values represent a remarkable red shift relative to **DTTB**, indicating the effective extension of the p–π* conjugation through the boron atom. The low absorbance of the long-wavelength band in **P1** compared with **P2** is likely attributable to torsional strain within the polymer backbone (*vide infra*). Thin-film absorption spectra were slightly red-shifted relative to the solution-state spectra (Fig. 7a), particularly for **P2**, suggesting the presence of intermolecular π–π interactions in the solid state. The electrochemical properties were evaluated using CV on polymer thin films (Fig. S12). As anticipated, both **P1** and **P2** possess low-lying LUMO energy levels (below −3.3 eV), validating their potential as n-type semiconductors. Notably, NDI copolymer **P1** exhibits a LUMO energy level of −3.87 eV, which is comparable to that of the archetypal n-type semiconductor polymer N2200 (−3.84 eV).[18] DFT calculations performed on oligomer models revealed that the **DTTB** and DPP units in **P2** exhibit a high degree of coplanarity (Fig. 7b). In contrast, the **DTTB** and NDI units in **P1** are significantly twisted, characterized by a large dihedral angle of approximately 50°. Reflecting these structural differences, both the HOMO and LUMO of **P2** are delocalized over both units (Fig. S13). Conversely, for **P1**, the

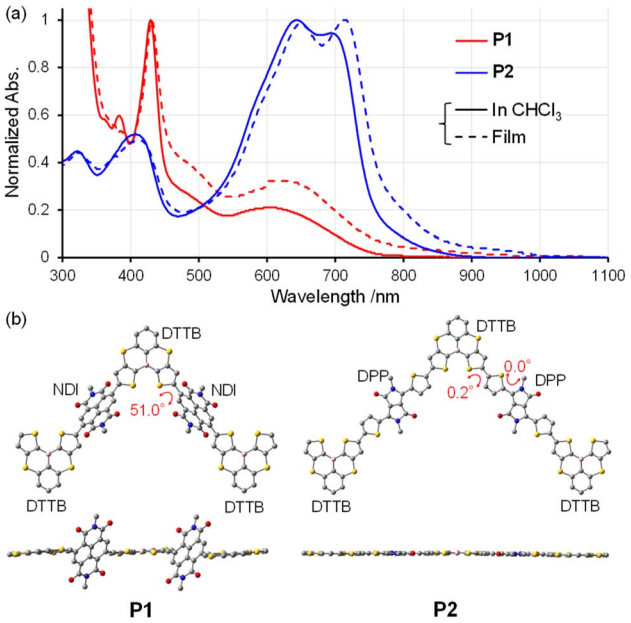

Fig. 7 (a) UV-vis absorption spectra of **P1** and **P2** in chloroform and as thin films. (b) Optimized geometries of the oligomer models for **P1** and **P2**.

HOMO is primarily localized on the **DTTB** units, whereas the LUMO is confined to the NDI units, which can be ascribed to the substantial steric twist between the two moieties.

Charge carrier transport properties

To evaluate the charge carrier transport properties of the polymers, organic field-effect transistors (OFETs) were fabricated using a top-gate/bottom-contact (TG/BC) architecture. Fig. S14 shows the transfer and output curves of the resulting OFETs, and Table 3 summarizes the corresponding device parameters. Both polymers exhibited V-shaped transfer curves under saturation conditions (source–drain voltage $V_d = \pm 100$ V) for both p- and n-channel operations, indicating ambipolar transport behavior. The emergence of p-type transport behavior, in addition to n-type, is likely attributable to the relatively high-lying HOMO energy levels of these polymers. **P2** demonstrated hole (μ_h) and electron (μ_e) mobilities of 8.2×10^{-3} and 1.1×10^{-3} cm^2 V^{-1} s^{-1}, respectively, which are more than one order of magnitude higher than those of **P1** ($\mu_h = 7.1 \times 10^{-5}$ cm^2 V^{-1} s^{-1}, $\mu_e = 3.4 \times 10^{-4}$ cm^2 V^{-1} s^{-1}). Although **P1** exhibits a lower μ_e than **P2**, its electron-to-hole mobility ratio (μ_e/μ_h) is significantly higher, reaching 4.8 for **P1** as opposed to 0.13 for **P2**, suggesting that **P1** possesses a pronounced preference for electron transport. Furthermore, in p-channel operation, **P1** exhibits a larger magnitude of threshold

Table 2 Properties of **P1** and **P2**

Polymer	M_n	M_w/M_n	T_d^5/°C [a]	λ_{abs}/nm [b]	E_g^{Opt}/eV [c]	HOMO/eV [d]	LUMO/eV [e]
P1	7,500	2.25	450	605 (618)	1.61	−5.67	−3.87
P2	32,600	1.87	424	644, 693 (649, 714)	1.44	−5.40	−3.33

[a] 5% Weight-loss temperature in N_2. [b] Absorption maxima in chloroform; thin-film values are shown in parentheses. [c] Optical band gap estimated from the absorption onset in chloroform. [d] HOMO = −4.8 − E_{ox}^{onset}. [e] LUMO = −4.8 − E_{red}^{onset}.

Table 3 OFET characteristics

	p-channel		n-channel		
Polymer	μ_h/cm^2 V^{-1} s^{-1} [a]	V_{th}/V [b]	μ_e/cm^2 V^{-1} s^{-1} [a]	V_{th}/V [b]	μ_e/μ_h [c]
P1	7.1×10^{-5} [$6.0 \times 10^{-5} \pm 9.2\times 10^{-6}$]	−44	3.4×10^{-4} [$2.8 \times 10^{-4} \pm 6.5\times 10^{-5}$]	55	4.8
P2	8.2×10^{-3} [$7.7 \times 10^{-3} \pm 5.5\times 10^{-4}$]	−16	1.1×10^{-3} [$1.0 \times 10^{-3} \pm 1.1 \times 10^{-4}$]	80	0.13

[a] μ_h and μ_e represent the maximum hole and electron saturation field-effect mobilities, respectively. The average values obtained from eight devices are given in brackets with standard deviations. [b] Threshold voltage. [c] Electron-to-hole mobility ratio.

voltage (V_{th}) (−44 V) than **P2** (−16 V), whereas in n-channel operation, **P1** shows a lower V_{th} (55 V) than **P2** (80 V). This enhanced n-channel behavior of **P1** relative to **P2** is most likely ascribed to its lower-lying LUMO energy level, which promotes more stable electron transport and facilitates efficient electron injection. Although it should be noted that these OFET devices were prepared and evaluated under different conditions, the carrier mobilities of **P1** and **P2** are higher than those of previously reported p–π* conjugated n-type semiconductors utilizing non-planarized triarylborane units.[19] Furthermore, considering that our previously reported copolymer of DTSB and DPP exhibited no semiconducting behavior,[11c] these results confirm that planarization of the boron unit is an effective strategy for enhancing charge transport performance.

Photovoltaic properties

We subsequently investigated the photovoltaic properties by fabricating all-polymer organic photovoltaics (OPVs) incorporating **P1** and **P2** as n-type semiconductors. The widely used donor material PTB7-Th (Fig. S15a) was selected as the p-type component. Active layers of *ca.* 100 nm thickness were spin-coated from 8 g L^{-1} chloroform solutions of PTB7-Th : **DTTB**-based polymer blends at a 1 : 1 weight ratio. Fig. S15b and S15c display the current density (*J*)–voltage (*V*) curves and the external quantum efficiency (EQE) spectra of the optimized cells, respectively. The corresponding photovoltaic parameters are summarized in Table S4. Although OPVs based on these polymers did not exhibit exceptional power conversion efficiencies (PCEs), the device utilizing **P1** achieved a PCE of 0.54%, confirming distinct photovoltaic characteristics. Although the maximum EQE values are relatively modest (~10%), a clear photoresponse in the absorption region corresponding to **P1** indicates that this polymer effectively contributes to the photoelectric conversion. In contrast, the PTB7-Th : **P2** cells exhibited negligible photovoltaic performance, likely ascribable to the relatively high-lying HOMO and LUMO energy levels of **P2**, which resulted in an insufficient energetic offset with PTB7-Th (Fig. S15a), thereby suppressing efficient charge transfer.

Polymer ordering in neat and blend films

Finally, to investigate polymer ordering in neat and blend films, grazing incidence X-ray diffraction (GIXD) measurements were conducted. Fig. 8 displays the two-dimensional (2D) GIXD patterns, along with the corresponding out-of-plane (solid lines) and in-plane (dotted lines) diffraction profiles for the neat films. In the neat films, **P1** exhibited no discernible diffraction peaks, indicating a predominantly amorphous nature. In contrast, **P2** displayed a distinct (010) diffraction peak along the q_z axis, attributed to π–π stacking and suggesting a predominantly face-on orientation. The corresponding π–π stacking distance (d_π) for **P2** was estimated to be 3.92 Å. The difference in crystallinity between the polymers can be rationalized by their respective polymer backbone conformations, as predicted by DFT calculations (Fig. 7b). Whereas **P1** adopts a highly bent and twisted backbone, **P2** features a less curved and more coplanar architecture. These structural features of **P2** likely contribute to the high charge carrier mobilities observed in the OFET devices. Furthermore, the low molecular weight of **P1** may contribute to its inferior carrier transport properties. In the PTB7-Th blend films, both polymers showed (010) diffraction peaks along the q_z axis (q_z = 1.72 and 1.68 Å^{-1} for **P1** and **P2**, respectively), again indicating a predominant face-on orientation (Fig. S16). The d_π values were determined to be 3.66 and 3.73 Å for the PTB7-Th : **P1** and PTB7-Th : **P2** blend films, respectively. Considering that **P1** is amorphous in the neat film and d_π of the neat **P2** film is 3.92 Å, the observed (010) diffractions in the blend films are likely attributable to the π–π stacking of PTB7-Th rather than the **DTTB**-based polymers. The low crystallinity of the **DTTB**-based polymers in the blend film is considered to be the primary cause of the low J_{SC} and FF observed in the corresponding OPV cells.

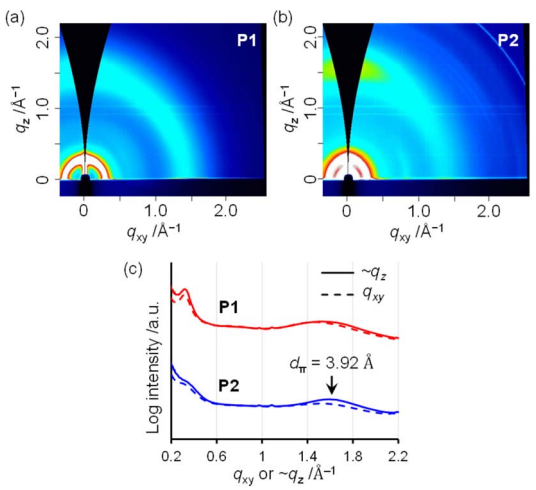

Fig. 8 2D GIXD patterns of neat polymer films of (a) **P1** and (b) **P2**. (c) Cross-sectional diffraction profiles extracted from the 2D GIXD patterns along the q_{xy} (solid line) and $-q_z$ (dashed line) axes.

Consequently, the OFET results demonstrate that rigid planarization can effectively resolve the inherent trade-off between chemical stability and intermolecular interactions in tricoordinate boron materials. By eliminating the need for bulky substituents while maintaining high stability, this design strategy enables efficient carrier transport in p–π* conjugated polymers, which has been difficult to achieve in non-planarized systems. However, the observed semiconducting properties of the **DTTB**-based polymers were modest, which is likely attributed to their low crystallinity. Since monomer structures with high curvature, such as **DTTB**, are known to impair polymer backbone linearity and thus reduce crystallinity.[20] Therefore, molecular designs aimed at minimizing curvature, for instance by altering the fusion orientation of the thiophene rings, will be essential to further enhance the semiconducting performance.

Conclusions

A new planarized triarylborane, **DTTB**, was developed by fusing benzene and thiophene rings onto thiaborin cores. **DTTB** is characterized by its perfect planar geometry and high chemical stability. Although **DTTB** is TADF-inactive, its intense low-temperature phosphorescence underscores its potential as a structural scaffold for new phosphorescent materials. By exploiting the facile deprotonation at the thiophene α-positions, we achieved the first synthesis of p–π* conjugated polymers incorporating planarized triarylborane units, representing a conceptual advance in the design of boron-containing materials. These polymers exhibited enhanced carrier mobilities compared with analogous p–π* conjugated polymers based on non-planar triarylborane units, thereby demonstrating that rigid planarization can be a strategy for resolving the inherent trade-off between chemical stability and intermolecular interactions. This work establishes a molecular design principle for improving the semiconducting properties of p–π* conjugated polymers without relying on bulky steric protection.

Author contributions

Yohei Adachi: conceptualization, writing – original draft, writing – review & editing, visualization, funding acquisition, supervision, project administration; Ryuji Matsuura: investigation, formal analysis, data curation, methodology; Hiroki Tobita: investigation; Tsubasa Mikie: investigation, formal analysis, writing – original draft, writing – review & editing; Itaru Osaka: resources, supervision; Joji Ohshita: funding acquisition, writing – review & editing, supervision.

Conflicts of interest

There are no conflicts to declare.

Data availability

CCDC 2538812 contains the supplementary crystallographic data for this paper.[21]

All data are available in the manuscript and in the supplementary information (SI). Supplementary information is available. See DOI: https://doi.org/10.1039/d6sc02594c.

Acknowledgements

This work was supported by JSPS KAKENHI (Grant Number JP22K14666). The 2D GIXD experiments were performed at BL13XU of SPring-8 with the approval of the Japan Synchrotron Radiation Research Institute (JASRI) (Proposal No. 2025A1652). The authors thank Dr T. Koganezawa (JASRI) for assistance with the 2D GIXD measurements.

References

1 (*a*) S. S. S. Shahnawaz, M. R. Nagar, R. A. K. Yadav, S. Gull, D. K. Dubey and J.-H. Jou, *J. Mater. Chem. C*, 2019, **7**, 7144; (*b*) P. Murugan, T. Hu, X. Hu and Y. Chen, *J. Mater. Chem. A*, 2022, **10**, 5044; (*c*) F. Zhang and C.-a. Di, *Chem. Mater.*, 2020, **32**, 2688.

2 (*a*) A. Wakamiya and S. Yamaguchi, *Bull. Chem. Soc. Jpn.*, 2015, **88**, 1357; (*b*) L. Ji, S. Griesbeck and T. B. Marder, *Chem. Sci.*, 2017, **8**, 846; (*c*) B. Chen and F. Jäkle, *Angew. Chem., Int. Ed.*, 2024, **63**, e202313379.

3 (*a*) X. Yin, J. Liu and F. Jäkle, *Chem. Eur J.*, 2021, **27**, 2973; (*b*) Y. Adachi, T. Nomura, S. Tazuhara, H. Naito and J. Ohshita, *Chem. Commun.*, 2021, **57**, 1316.

4 Z. Zhou, A. Wakamiya, T. Kushida and S. Yamaguchi, *J. Am. Chem. Soc.*, 2012, **134**, 4529.

5 Representative examples of pioneering works(*a*) Y. Kitamoto, T. Suzuki, Y. Miyata, H. Kita, K. Funaki and S. Oi, *Chem. Commun.*, 2016, **52**, 7098; (*b*) T. Hatakeyama, K. Shiren, K. Nakajima, S. Nomura, S. Nakatsuka, K. Kinoshita, J. Ni, Y. Ono and T. Ikuta, *Adv. Mater.*, 2016, **28**, 2777; (*c*) S. Nakatsuka, H. Gotoh, K. Kinoshita, N. Yasuda and T. Hatakeyama, *Angew. Chem., Int. Ed.*, 2017, **56**, 5087.

6 (*a*) A. Escande and M. J. Ingleson, *Chem. Commun.*, 2015, **51**, 6257; (*b*) E. von Grotthuss, A. John, T. Kaese and M. Wagner, *Asian J. Org. Chem.*, 2018, **7**, 37; (*c*) M. Hirai, N. Tanaka, M. Sakai and S. Yamaguchi, *Chem. Rev.*, 2019, **119**, 8291; (*d*) M. Schnitzlein and F. Würthner, *ChemistryEurope*, 2025, **3**, e202500135.

7 (*a*) H. J. Kim and T. Yasuda, *Adv. Opt. Mater.*, 2022, **10**, 2201714; (*b*) M. Mamada, M. Hayakawa, J. Ochi and T. Hatakeyama, *Chem. Soc. Rev.*, 2024, **53**, 1624.

8 (*a*) K. Matsuo, S. Saito and S. Yamaguchi, *J. Am. Chem. Soc.*, 2014, **136**, 12580; (*b*) F. Miyamoto, S. Nakatsuka, K. Yamada, K. Nakayama and T. Hatakeyama, *Org. Lett.*, 2015, **17**, 6158; (*c*) T. Kushida, A. Shuto, M. Yoshio, T. Kato and S. Yamaguchi, *Angew. Chem., Int. Ed.*, 2015, **54**, 6922; (*d*) T. Kushida, S. Shirai, N. Ando, T. Okamoto, H. Ishii, H. Matsui, M. Yamagishi, T. Uemura, J. Tsurumi, S. Watanabe, J. Takeya and S. Yamaguchi, *J. Am. Chem. Soc.*, 2017, **139**, 14336; (*e*) W. Sun, J. Guo, Z. Fan, L. Yuan, K. Ye, C. Dou and Y. Wang, *Angew. Chem., Int. Ed.*, 2022, **61**, e202209271.

9 Y. Ren and F. Jäkle, *Dalton Trans.*, 2016, **45**, 13996.

10 (*a*) S. Saito, K. Matsuo and S. Yamaguchi, *J. Am. Chem. Soc.*, 2012, **134**, 9130; (*b*) M. Sakai, M. Mori, M. Hirai, N. Ando and S. Yamaguchi, *Chem. Eur J.*, 2022, **28**, e202200728; (*c*) B. Du, Y. Wu, X. Wang, H. Tian, S. Shao and L. Wang, *Chem. Sci.*, 2024, **15**, 19432; (*d*) D. Lee, J. Moon, S. Kim and J. Y. Lee, *Adv. Mater.*, 2026, **38**, e21668; (*e*) X. Y. Wang, F. D. Zhuang, R. B. Wang, X. C. Wang, X. Y. Cao, J. Y. Wang and J. Pei, *J. Am. Chem. Soc.*, 2014, **136**, 3764.

11 (*a*) Y. Adachi, M. Sakabe, T. Nomura and J. Ohshita, *Polym. J.*, 2023, **55**, 489; (*b*) Y. Adachi, R. Matsuura and J. Ohshita, *Organometallics*, 2024, **43**, 829; (*c*) Y. Adachi, R. Matsuura, M. Sakabe, H. Tobita, H. Murakami and J. Ohshita, *Polym. Chem.*, 2025, **16**, 2751.

12 H. Uoyama, K. Goushi, K. Shizu, H. Nomura and C. Adachi, *Nature*, 2012, **492**, 234.

13 N. Mataga, Y. Kaifu and M. Koizumi, *Bull. Chem. Soc. Jpn.*, 1956, **29**, 465.

14 Z. Chen, C. S. Wannere, C. Corminboeuf, R. Puchta and P. von Ragué Schleyer, *Chem. Rev.*, 2005, **105**, 3842.

15 F. Chen, L. Zhao, X. Wang, Q. Yang, W. Li, H. Tian, S. Shao, L. Wang, X. Jing and F. Wang, *Sci. China Chem.*, 2021, **64**, 547.

16 S. Soléa and F. P. Gabbaï, *Chem. Commun.*, 2004, 1284.

17 P. Erdmann, J. Leitner, J. Schwarz and L. Greb, *ChemPhysChem*, 2020, **21**, 987.

18 L. Gao, Z.-G. Zhang, L. Xue, J. Min, J. Zhang, Z. Wei and Y. Li, *Adv. Mater.*, 2016, **28**, 1884.

19 (*a*) B. Meng, Y. Ren, J. Liu, F. Jäkle and L. Wang, *Angew. Chem., Int. Ed.*, 2018, **57**, 2183; (*b*) Y. Yu, B. Meng, F. Jäkle, J. Liu and L. Wang, *Chem. Eur J.*, 2020, **26**, 873; (*c*) Y. Yu, C. Dong, A. F. Alahmadi, B. Meng, J. Liu, F. Jäkle and L. Wang, *J. Mater. Chem. C*, 2019, **7**, 7427–7432.

20 (*a*) R. Rieger, D. Beckmann, A. Mavrinskiy, M. Kastler and K. Müllen, *Chem. Mater.*, 2010, **22**, 5314; (*b*) I. Osaka, T. Abe, S. Shinamura and K. Takimiya, *J. Am. Chem. Soc.*, 2011, **133**, 6852.

21 CCDC 2538812: Experimental Crystal Structure, 2026, DOI: 10.5517/ccdc.csd.cc2r6v50.